Research Article Vol. 12, No. 5 / 1 May 2021 / Biomedical Optics Express 2841

Biomedical Optics EXPRESS

Quasi-distributed fiber optic sensor-based control system for interstitial laser ablation of tissue: theoretical and experimental investigations

LEONARDO BIANCHI, SANZHAR KORGANBAYEV, ANNALISA ORRICO, MARTINA DE LANDRO, AND PAOLA SACCOMANDI*

Department of Mechanical Engineering, Politecnico di Milano, Milan, Italy
*paola.saccomandi@polimi.it

Abstract: This work proposes the quasi-distributed real-time monitoring and control of laser ablation (LA) of liver tissue. To confine the thermal damage, a pre-planning stage of the control strategy based on numerical simulations of the bioheat-transfer was developed to design the control parameters, then experimentally assessed. Fiber Bragg grating (FBG) sensors were employed to design the automatic thermometry system used for temperature feedback control for interstitial LA. The tissue temperature was maintained at a pre-set value, and the influence of different sensor locations (on the direction of the beam propagation and backward) on the thermal outcome was evaluated in comparison with the uncontrolled case. Results show that the implemented computational model was able to properly describe the temperature evolution of the irradiated tissue. Furthermore, the realized control strategy allowed for the accurate confinement of the laser-induced temperature increase, especially when the temperature control was actuated by sensors located in the direction of the beam propagation, as confirmed by the calculated fractions of necrotic tissues (e.g., 23 mm^3 and 53 mm^3 for the controlled and uncontrolled LA, respectively).

© 2021 Optical Society of America under the terms of the OSA Open Access Publishing Agreement

1. Introduction

Electromagnetic-based thermal techniques are currently widely investigated as minimally invasive treatments for solid tumor removal [1]. Among the diverse ablative procedures [2–4], laser ablation (LA) has raised considerable attention for clinical applications [5]. Typical advantages are the capability to deliver the therapeutic laser beam through small and flexible optical fibers able to target deep-seated organs [6], and the compatibility with diagnostic imaging techniques for therapy guidance [7]. Furthermore, the reduced invasiveness and pain, associated with this ablative procedure, could reduce the recovery time, and could represent an alternative to surgical resection [8]. In this concern, interstitial LA, based on the irreversible thermal damage of neoplasms due to photothermal conversion of near-infrared (NIR) light into heat, has shown promising results for the local treatment of liver [9], brain [10,11], prostate [12], lung [13], pancreas [14] and breast tissue [15].

However, LA still holds some downsides which prevent the inclusion of this technique into clinical practice, such as the charred tissue at the applicator tip due to high-temperature gradient (>50 °C/mm) and consequent overheating [16], and the potential risk of irreversible injury to the surrounding healthy structures. Indeed, the maintenance of thermal coagulation and necrosis within the selected tissue margins, surrounding the targeted tumor shape, is often challenging. This concern can be ascribed to the absence of a real-time temperature feedback control strategy and the lack of dedicated pre-treatment planning which are responsible for the inaccuracy of the overall thermal procedure [6,17]. The evaluation and control of the spatially resolved tissue temperature evolution are of paramount importance as the prime factors triggering the damage

#419541 https://doi.org/10.1364/BOE.419541
Journal © 2021 Received 12 Jan 2021; revised 12 Mar 2021; accepted 23 Mar 2021; published 21 Apr 2021

Biomedical Optics EXPRESS

to tumorous cells and allowing for a safety temperature margin around the lesion to prevent undesired damage. Temperatures of 60 °C are typically known to induce instantaneous and irreversible thermal damage, due to protein denaturation, collapses of the cellular membranes, and impairment of mitochondrial function. Conversely, temperatures comprised between 41–45 °C typically refer to the so-called sublethal damage as reversible injury occurs [18]. However, if these temperature values are kept for a sufficiently long time, the thermal effect can still be achieved in the tissue. In this regard, the synergistic role of temperature and time in the induction of thermal damage is described by well-known models such as Cumulative Equivalent Minutes at 43 °C (CEM43) and Arrhenius [19,20].

Different strategies have been implemented for the local monitoring of the biological tissue temperature and to confine the attained temperature values within specific ranges during thermal therapies. Most of the works in this field employ standard sensors, such as thermocouples and thermistors [21–23]. These works usually rely on the use of single-point measurement to perform the temperature control strategy, hence leading to increased invasiveness when more sensors are needed for performing both control and monitoring in the tissue. In other cases, thermometric approaches based on diagnostic imaging are also proposed for regulating heating, eliminating tissue carbonization, and protecting fiber optic applicators [24]. These techniques are interesting for the estimation of the thermal dose based on the spatially resolved measured temperature map, but they are still far to be considered as routinely and widely available approaches for all the thermal procedures in clinical settings. On the contrary, fiber optic technology is an advantageous alternative to conventional sensing methods. Thanks to the possible multipoint temperature measurements and low heat conductivity, fiber optic sensors are suitable for laser-assisted therapies [25]. Particularly, fiber Bragg grating (FBG) sensors embedded into biocompatible optical fibers are attractive for quasi-distributed sensing during thermal treatments due to also the multiplexing capability [26,27]. Recently, our group has developed an FBG-based closed-loop temperature control algorithm able to control tissue temperature during contactless irradiation in order to maintain the desired set temperature at the margins of the targeted zone [28]. In this preliminary experimental work, the use of FBG arrays allowed for quasi-distributed monitoring, able to also provide information about the spatial temperature distribution reached in the tissue. Although the results demonstrated the feasibility of FBGs control to confine the temperature in a specific area, this study was limited to a superficial treatment without any assessment of the pre-planning procedural settings parameters. Indeed, contactless LA was used as a first step to validate our strategy, but it remains far from clinical settings.

To move towards a real application of LA, an efficient control strategy should be investigated in a contact modality (i.e., interstitial) and supported by simulation-based pre-planning models [29]. These tools allow optimizing the control parameters, e.g., the appropriate laser dose, the sensor position, to attain the required pre-planning of the experiments. This approach has been adopted also in some excellent recent studies, which are still using some simplifications, such as the non-dependency of the tissue optical properties with coagulation [29], or the low sensing resolution of the temperature-based modulation technique [30].

In the present study, we combine the implementation of a pre-planning control stage with the use of FBGs for temperature feedback control of interstitial LA and for model validation. Therefore, a computational model of the bioheat transfer in biological tissue has been implemented for numerically assessing the volumetric heat distribution and the associated tissue changes. Highly dense FBG arrays have been utilized to spatially confine the thermal distribution at specific locations from the laser applicator, assuring the maintenance of pre-set margins of ablation. Additionally, the effects of the position of the controlling sensors on the final thermal outcome have been investigated from both theoretical and experimental viewpoints.

Biomedical Optics EXPRESS

2. Materials and methods

2.1. Laser irradiation of the tissue phantom

To evaluate the efficacy of the developed interstitial LA control approach, experiments on *ex vivo* porcine liver tissue were performed. We selected the liver tissue since it is well characterized in terms of optical and thermal properties [31–33]. Hence, it can be a valuable model for studying the control strategy for interstitial LA, from both a theoretical and empirical viewpoint. The fresh swine liver tissue was obtained from a local butchery on the same day of the experiments, and it was kept at 4 °C before the tests. An 808 nm diode laser (LuOcean Mini 4, Lumics, Berlin, Germany) was used to irradiate the liver at room temperature. The initial tissue temperature, $T_0 = 23$ °C, was measured with a type K thermocouple. Laser light was conveyed by a flexible quartz optical fiber inserted into the liver tissue. The laser power of 2 W was delivered for 120 s during each ablation test. This choice is motivated by the use of the *ex vivo* liver, where the absence of heat-sink effect due to blood perfusion could lead to high temperatures close to the applicator tip, especially in uncontrolled experiments. Moreover, in all the controlled tests, the control logic resulted to be activated under these settings.

2.2. Fiber optic sensors

To provide temperature measurements for LA control, four custom-made FBG array fiber-optic sensors were employed. The polyimide coating of the utilized fibers provides a high-temperature resistance (up to 400 °C) and low thermal conductivity properties [34–36], important for accurate measurements near the laser applicator tip, where temperature gradient can reach 50 °C/mm [16]. Each FBG array has 40 gratings and the following properties: a grating length equal to 1.19 mm, and a 0.01 mm edge-to-edge distance between gratings. As a result, the arrays have a spatial resolution of 1.2 mm and the total sensing length equal to 48 mm. The thermal sensitivity of the sensors is $(7.43 \pm 0.01)\times10^{-6}$ °C^{-1}. More details about sensors' fabrication, characteristics, and calibration are provided in the previous work of our group [28]. The principle of FBG temperature reconstruction is based on the phenomenon of Bragg wavelength shift induced by the applied temperature. As a result, peak tracking of FBG reflected spectrum allows measurements of temperature change along the FBG structure. To measure the reflection spectra of the FBG arrays, Micron Optics si255 interrogation unit (Micron Optics, Atlanta, USA) with 100 Hz sampling rate was utilized. The data from Micron Optics were analyzed in real-time on a computer by the custom LabVIEW program developed to obtain real-time temperature profiles along the connected FBG arrays and use temperature information for controlling the laser diode power settings.

2.3. Experimental arrangement

To guarantee accurate positioning of the laser applicator and the sensors inside the liver, a custom-made plexiglass box was used (Fig. 1(a) and Fig. 1(b)) [26]. The box with holes positioned at a 2 mm distance from each other on all sides of the box allows a wide range of different positionings of the sensors and the laser applicator. Figure 1 illustrates the experimental arrangement used for all tests: the central hole was used for the laser applicator (blue circle in Fig. 1(c)), and four holes positioned at 4 mm distances from the central hole were used to insert FBG arrays parallel to the applicator (green circles in Fig. 1(c)). The fibers were sequentially inserted into the tissue. A needle (18 gauge) was utilized to insert FBG array fibers into hepatic tissue and it was removed before proceeding with the laser irradiation. Each insertion was manually performed and needed approximately 2 min.

Biomedical Optics EXPRESS

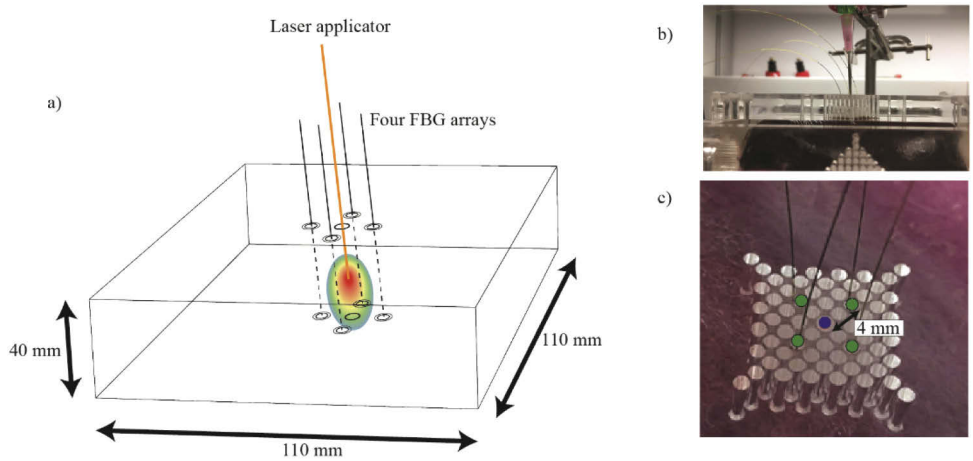

Fig. 1. Experimental setup: (a) schematics of the positioning of laser applicator and fiber Bragg grating (FBG) arrays in the liver placed in plexiglass box; (b) photo of the experimental box employed for maintaining the position of the fibers; (c) close-up of the box with labeled holes for the placement of the fiber optic sensors (green color, diameter of the hole equal to 1 mm) and the laser applicator (blue color, diameter of the hole equal to 1.5 mm) inside the *ex vivo* liver.

2.4. Control logic

The quasi-distributed sensing property of FBG arrays allows for different temperature control approaches depending on the arrangement of the applicator and the sensors, and the controlled parameter of the temperature (e.g., maximum temperature, the temperature at a specific position, overall temperature profile). The algorithm for interstitial ablation developed in this work aims to maintain the temperatures at the margins of the treated region below the pre-set value. The treated region is defined by 4 parallel FBG arrays and the plane z_d which is perpendicular to the laser applicator axis (that is the z-axis) and positioned at a distance d from the applicator tip (Fig. 2(a)). This approach allows controlling the temperature distribution at any distance from the applicator tip, which can be essential in case of the presence of affecting factors at specific positions, such as blood vessels, tumor's edge, or healthy tissue that should be preserved undamaged.

The algorithm consists of three main stages: (*i*) pre-setting: setting of the input parameters based on simulation outcome, before the start of LA; (*ii*) alignment phase; (*iii*) ON-OFF control of laser irradiation based on temperature measurements.

For the first stage, after positioning of the sensors and the laser applicator in the box, three parameters are needed to be set before the LA procedure: the laser power P, the set temperature T_S and the controlled distance d. T_S is the maximum tissue temperature maintained by the control algorithm on the selected zone. This zone is defined by the z_d plane perpendicular to the laser applicator and 4 point-measurements, from the 4 FBG arrays, located within the defined plane; the position of the z_d plane (which lies in the xy plane) is defined by the controlled distance d (Fig. 2(a)). The efficacy of the pre-set values for the aimed ablation is validated by the simulations before the LA procedure. Five different planes of interest z_d were considered at d equal to -3 mm, -2 mm, 0 mm, +2mm, and +3 mm, where the positive sign indicates that the same direction of the laser beam irradiation is considered.

Automatic spatial alignment of FBGs' temperature profiles is utilized in the second stage of the algorithm (Fig. 2(b)). The alignment employs the centroid method that adjusts the centers of temperature profiles measured by each FBG array along the z-direction [26]. Particularly,

Biomedical Optics EXPRESS

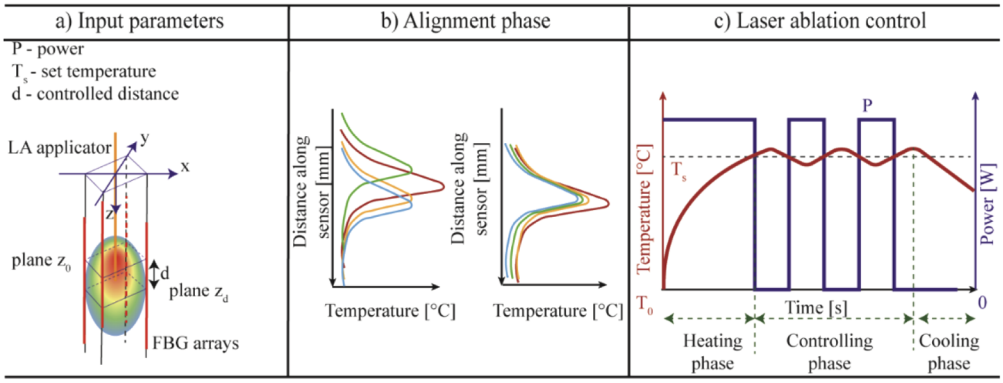

Fig. 2. Laser ablation (LA) control: (a) pre-set of input parameters: laser power P, set temperature T_S, and controlled distance d to define the controlled plane z_d. Red lines illustrate the sensing regions of fiber Bragg grating (FBG) arrays that are not spatially aligned; (b) alignment of measured temperature profiles for four FBG arrays. Peaks of measured temperatures correspond to plane z_0; (c) ON-OFF control of maximum temperature measured at the plane z_d: the graph depicts the power and temperature evolution. T_0 represents the room temperature.

the centroid method is automatically implemented at the moment when maximum temperatures measured by each FBG array reach 6 °C when a clear Gaussian temperature profile can be observed. The alignment is performed in one LabVIEW iteration (~3 ms).

The developed algorithm implemented in LabVIEW utilizes an ON-OFF control logic: the laser power P is switched off if the measured peak temperature is equal to or higher than the set temperature T_S, and switched on if the measured peak temperature is less than T_S (Fig. 2(c)). Comparison of the 4 measured temperature values on the z_d plane and T_S is performed each $\Delta\tau$ seconds:

$$\begin{cases} P = 0W \quad if \quad T - T_s \geq 0 \quad \wedge \quad t = n \cdot \Delta\tau \quad n \in \mathbb{N} \\ P = 2W \quad if \quad T - T_s < 0 \quad \wedge \quad t = n \cdot \Delta\tau \quad n \in \mathbb{N} \end{cases} \tag{1}$$

The temperature comparison period $\Delta\tau$ was set to 0.5 s to avoid possible overloading of the laser diode equipment [37]. It is important to highlight that the system response is delayed due to $\Delta\tau$, and, to more extent, due to the delayed temperature response at a 4 mm distance from the applicator, due to the heat conduction in the treated tissue. T_S can be set by the user; in this study, for both simulations and experiments, it was set at 40 °C to ensure, at the selected spatial location, the avoidance of a temperature value able to activate the tissue immune responses that typically occur in the range between 42 °C and 45 °C [38].

3. Computational model of temperature-controlled interstitial laser ablation

3.1. Theoretical model

The laser-induced thermal response of *ex vivo* biological tissue was modeled by the heat diffusion equation [39], expressed as

$$\rho \cdot c \cdot \frac{\partial T}{\partial t} + \nabla(-k\nabla T) = Q_{laser} \tag{2}$$

where ρ (kg·m^{-3}), c (J·kg^{-1}·K^{-1}) and k (W·m^{-1}·K^{-1}) are the density, the specific heat, and the thermal conductivity of tissue, respectively; T (K) is the tissue temperature and Q_{laser} (W·m^{-3}) is

Biomedical Optics EXPRESS

the heat generation term due to laser-tissue interaction. The contribution of the metabolic heat source and the blood perfusion were placed equal to zero in the present model, for simulating the LA procedure on *ex vivo* tissue. The penetration of laser light in the tissue and the deposited thermal energy due to laser light absorption in the biological media can be addressed according to the Beer-Lambert law [14]:

$$Q_{laser} = \alpha_a \cdot I_r \cdot e^{-\alpha_a \cdot d_t} \tag{3}$$

where α_a (m^{-1}) is the absorption coefficient, d_t (m) is the axial depth in tissue, and I_r ($W \cdot m^{-2}$) is the laser irradiance, defined as a function of radial distance since the spatial beam profile is assumed to be a 2-D Gaussian distribution with a standard deviation of σ (m). The following equation reports the expression of I_r:

$$I_r = \frac{P}{2\pi\sigma^2} exp\left(-\frac{r^2}{2\sigma^2}\right) \tag{4}$$

where P (W) is the power of the continuous-wave mode laser emitter and r (m) is the radial distance. In the present model, a laser radiation wavelength comprised within the so-called *therapeutic window*, i.e., 808 nm, was adopted. Hence, considering the interaction of NIR laser light with biological materials, typically defined as turbid media, the scattering cannot be neglected in comparison with the linear absorption phenomenon [14]. Thus, the effective attenuation coefficient, α_{eff} (m^{-1}), based upon diffusion approximation [40], was introduced to consider both the scattering and the absorption contributions:

$$\alpha_{eff} = \sqrt{3\alpha_\alpha(\alpha_\alpha + \alpha_s(1-g))} \tag{5}$$

where g and α_s (m^{-1}) are respectively the anisotropy and the scattering coefficient. Therefore, the absorption coefficient α_a in Eq. (3) was replaced with the effective attenuation coefficient α_{eff} of Eq. (5). The optical properties of the hepatic tissue were considered to change according to the portion of the damaged tissue (PDT) and were defined as follows:

$$\alpha_a = \alpha_{a,n} \cdot (1 - PDT) + \alpha_{a,c} \cdot PDT \tag{6}$$

$$\alpha_s = \alpha_{s,n} \cdot (1 - PDT) + \alpha_{s,c} \cdot PDT \tag{7}$$

$$g = g_n \cdot (1 - PDT) + g_c \cdot PDT \tag{8}$$

where $\alpha_{a,n}$ (m^{-1}), $\alpha_{s,n}$ (m^{-1}) and g_n are respectively the absorption, scattering, and anisotropy coefficients of native tissue, while $\alpha_{a,c}$ (m^{-1}), $\alpha_{s,c}$ (m^{-1}) and g_c are the absorption, scattering, and anisotropy coefficients of the coagulated tissue [22,41].

To assess the thermal damage during the laser irradiation procedure, the Arrhenius equation [39] was considered in the model. The degree of tissue injury $\theta(r,t)$, which is dependent on temperature and exposure time, was expressed as:

$$\theta(r,t) = \theta_0 + A_f \cdot \int_0^{\tau_{irr}} (1-\theta)^{n_p} \cdot exp\left(-\frac{E_a}{R \cdot T}\right) dt \tag{9}$$

where θ_0 is the initial degree of tissue injury, A_f (s^{-1}) is the frequency factor, τ_{irr} (s) is the total irradiation time, n_p is the polynomial order, E_a ($J \cdot mol^{-1}$) is the denaturation activation energy, R ($J \cdot mol^{-1} \cdot K$) is the universal gas constant, and T (K) is the absolute temperature in tissue. The portion of damaged tissue, PDT, is therefore calculated based on the degree of tissue injury θ, according to [42]:

$$PDT = min(max(\theta, 0), 1) \tag{10}$$

Table 1 reports the optical properties of native and coagulated liver tissue and the parameters utilized in the Arrhenius model.

Biomedical Optics EXPRESS

Table 1. Optical properties of swine hepatic tissue (native and coagulated) and parameters utilized for the Arrhenius thermal damage model.

Optical properties of porcine liver tissue					
Absorption coefficient, α_a (m^{-1})		**Scattering coefficient, α_s (m^{-1})**		**Anisotropy factor, g**	
Native	Coagulated	Native	Coagulated	Native	Coagulated
0.73 [32]	0.88 [32]	55 [32]	380.3 [32]	0.93 [32]	0.9 [32]
Parameters for the Arrhenius thermal damage model					
Frequency factor, A_f (s^{-1})		**Activation energy, E_a ($J \cdot mol^{-1}$)**		**Universal gas constant, R ($J \cdot mol^{-1} \cdot K$)**	
$5.5 \cdot 10^{41}$ [33]		$2.77 \cdot 10^{5}$ [33]		8.314 [33]	

To accurately predict the temperature distribution of the target tissue, the density ρ, the heat capacity c, and the thermal conductivity k of the porcine liver tissue were considered temperature-dependent. The trend of heat capacity and thermal conductivity were attained from [31] and the dynamic changes of density were expressed according to the following equation:

$$\begin{cases} \rho(T) = 1000 \cdot (1.3 - 0.3 \cdot k_\rho \cdot m_w) \\ k_\rho = 1 - 4.98 \cdot 10^{-4} \cdot (T - 20) \end{cases} \tag{11}$$

in which m_w indicates the water mass percentage in hepatic tissue, i.e., ~69% [41].

3.2. Numerical simulation

The finite element method (FEM)-based solver, COMSOL Multiphysics (COMSOL, Inc., Burlington, MA, USA) was adopted for solving the numerical model of the temperature-controlled LA procedure, performed on *ex vivo* porcine tissue. The simulation geometry concerned the modeling of the porcine liver tissue phantom (a cylinder of 5.5 cm in radius and 3 cm in thickness), the laser applicator, which was positioned along the central z-axis of the cylinder, and 4 pass-through FBG arrays located according to the experimental setup (Fig. 3(a)). Table 2 shows the dimensions of the adopted laser fiber applicator and of the FBG sensors, which are constituted by an outer polyimide coating and a silica glass core. Moreover, it reports the physical properties adopted for the materials characterizing the FBG sensors [43].

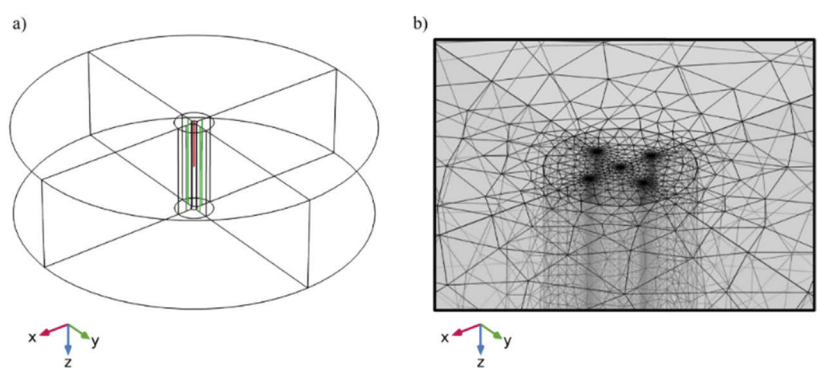

Fig. 3. (a) Geometry of the implemented model for feedback-controlled interstitial ablation simulation: laser applicator (red) and FBG array sensors (green) embedded in hepatic tissue are shown. (b) Close-up of the central part of the mesh utilized in the implemented model, with a minimum mesh size of 0.01 mm.

The COMSOL built-in free mesh generator was employed to generate free tetrahedral mesh elements for the physical domain discretization, with a minimum mesh size of 0.01 mm (Fig. 3(b)).

Biomedical Optics EXPRESS

Table 2. Dimensions of laser fiber and fiber Bragg grating (FBG) sensors and physical properties of the materials constituting the FBG arrays.

Dimensions of laser fiber and FBG sensors		
	Size (radius)	
Laser fiber applicator	0.1500 mm	
Polyimide coating of the FBG sensor	0.0775 mm	
Silica glass of the FBG sensor	0.0625 mm	
Physical properties of FBG materials		
Property	Polyimide	Silica glass
Absorption coefficient	0 cm^{-1}	10^{-5} cm^{-1}
Thermal conductivity	0.12 $W \cdot m^{-1} \cdot K^{-1}$	1.1 $W \cdot m^{-1} \cdot K^{-1}$
Density	1.42 $g \cdot cm^{-3}$	2.17 $g \cdot cm^{-3}$
Heat capacity	1.09 $J \cdot g^{-1} \cdot K^{-1}$	680 $J \cdot g^{-1} \cdot K^{-1}$

The numerical resolution of all the implemented simulations has been performed on an Intel Core i7-9800X workstation (3.8 GHz clock speed and 64.0 GB RAM).

4. Results

4.1. Simulation results

Figure 4 shows the temperature distribution for the different case-studies, namely, the uncontrolled procedure, and the LA control based on the comparison between the setpoint temperature T_s and the temperature assessed at different z_d planes with d equal to -3 mm, -2 mm, 0 mm, +2 mm, and +3 mm. For each displayed figure, the left semi-figure depicts the thermal values comprised between T_s (40 °C) and the maximum temperature obtained in the biological tissue. In the right part of each image, the corresponding volumes of hepatic tissue characterized by temperatures ≥ 40 °C (volume in yellow) and ≥ 60 °C (volume in brown) are also shown. The latter temperature was displayed as typically identified as the threshold value at which instantaneous thermal damage occurs in biological tissues [44]. The displayed spatial temperature profiles concern the heat distribution immediately before the laser source was turned off for the first time, thus, in case of controlled ablations, when the control phases initiate. This choice aims at attaining comparable thermal results among the different LA controls, based on the different locations. For all the cases, the maximum temperature is reached close to the applicator tip, where temperatures above 300 °C are observed. The uncontrolled laser irradiation shows the highest temperature values compared to all control cases. Furthermore, in this case, temperatures equal to 40 °C extend up to 1.76 mm away from the cylindrical region of tissue comprised between the laser tip and the location of the FBG sensors. In Fig. 4, the aforementioned distance between the point corresponding to the maximum extent at which temperatures of 40 °C can be found and the closest FBG sensor is indicated as r_{ext}. In case of temperature feedback control based on the comparison with the temperature at d equal to -3 mm, -2 mm, i.e., backward to the delivered laser beam, r_{ext} results equal to 0.73 mm and 0.22 mm, for d equal to -3 mm, -2 mm, respectively. For the control performed at d equal to +3 mm, +2 mm, i.e., along the laser beam propagation, the values of r_{ext} correspond to 0.49 mm and 0.13 mm, accordingly. Conversely, concerning the temperature control based upon the comparison at $d = 0$ mm, temperatures of 40 °C remain confined to the volume comprised between the laser applicator and the modeled FBG optical fibers.

Among all the considered cases, the uncontrolled LA shows the maximum volume of liver tissue at temperatures ≥ 40 °C, i.e., 509.2 mm^3. The control performed at $d = -3$ mm and

Biomedical Optics EXPRESS

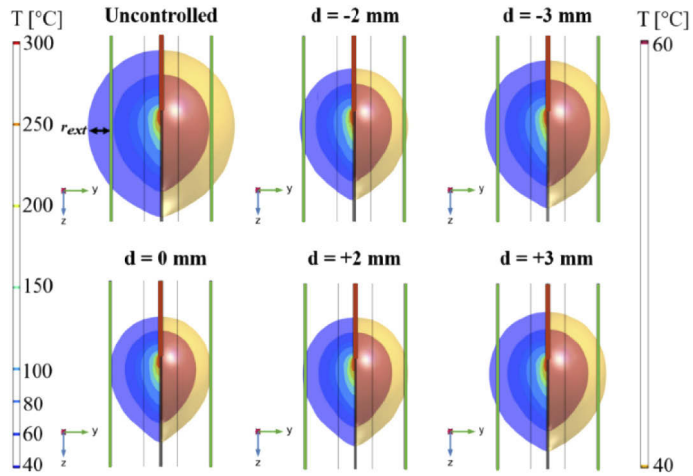

Fig. 4. Simulated temperature distribution for the different case-studies of interstitial thermal ablation, i.e., the uncontrolled procedure, and the control based on the comparison between the setpoint temperature T_s (40 °C) and the temperature assessed at the different d values, equal to -3 mm, -2 mm, 0 mm, +2 mm, and +3 mm. The heat distributions refer to the instant of time immediately before the laser source was turned off for the first time. For each figure, the left semi-figure depicts the thermal values comprised between T_s and the maximum attained temperature, whereas, in the right part, the corresponding volumes of tissue associated with temperatures ≥ 40 °C (yellow) and ≥ 60 °C (brown) are displayed.

$d = +3$ mm produced volumes of tissues at temperature ≥ 40 °C of 276.3 mm^3 and 225.6 mm^3, respectively. Smaller volumes of biological tissue heated up to temperatures equal to and over 40 °C refer to the control performed at 2 mm since for $d = -2$ mm and $d = +2$ mm, values of 192.8 mm^3 and 175.7 mm^3 are respectively shown. The smallest volume of tissue at 40 °C is attained in case of the temperature controlled based upon the comparison at $d = 0$ mm, i.e., 155.9 mm^3. Similarly, the values of tissue volume characterized by temperatures ≥ 60 °C are lower for $d = 0$ mm, and progressively increase for $d = +2$ mm and $d = -2$ mm, $d = +3$ mm and $d = -3$ mm, up to the maximum value of 132.6 mm^3, concerning the uncontrolled case. The previous analysis shows that, considering the same distances from the laser tip, temperatures remain more confined when the control is performed based on sensing locations in the forward direction of the beam propagation, compared to the corresponding locations set backward. Moreover, the closer the location of the controlling point to the laser applicator, the smaller the extent of temperatures over the setpoint value. Additionally, considering the temperature trend over time (Fig. 5), two relevant factors should be taken into account when evaluating the implemented control strategy. Firstly, since in the simulation the temperature values attained in the biological tissue undergoing LA and the setpoint temperatures are compared every $\Delta\tau = 0.5$ s, the time which elapses between when the setpoint temperature is exceeded and the laser source is turned off can cause a short delay in the control system (green circle of Fig. 5(b)). Secondly, the heat diffusion due to the tissue thermal properties once the laser is switched off can cause a response delay before the tissue temperature starts decreasing. Therefore, a consequent temperature overshoot can be observed (Fig. 5(b)).

Figure 6 depicts the temperature evolution over time for the different control cases. Considering the same distances from the laser tip, smaller overshoots are registered when the control is performed based on sensing locations placed backward to the beam propagation. Indeed, for the control performed upon the comparison of temperature at $d = -3$ mm and $d = -2$ mm, the overshoots (1.3 °C and 1.8 °C) are slightly lower than the values for the control performed based

Biomedical Optics EXPRESS

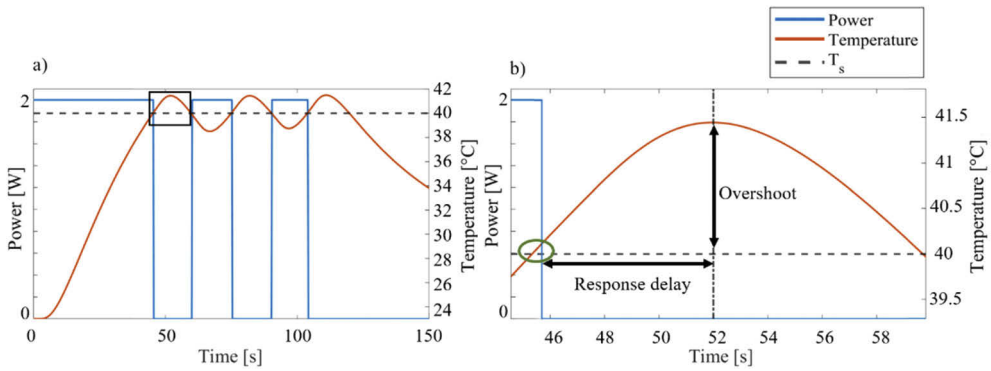

Fig. 5. (a) Power and temperature profiles attained by the simulation of temperature feedback-controlled interstitial laser irradiation of liver tissue. (b) Close-up on the simulated power and temperature evolution over time (corresponding to the black rectangle of figure a) to show an example of the small delay in the control system which can occur due to the time which elapses between when the setpoint temperature is exceeded and when the laser source is turned off (green circle), since the measured and the setpoint temperatures are compared every $\Delta\tau = 0.5$ s. The response delay after the simulated laser power is switched off and the associated temperature overshoot are also shown.

on the temperature at $d = +3$ mm and $d = +2$ mm (1.4 °C and 2.0 °C). Conversely, the response delay results higher when the control is performed based on sensing locations set behind the laser beam. That corresponds to 6.2 s and 5.8 s for $d = -3$ mm and $d = +3$ mm, respectively, and 5.1 s and 5.0 s for $d = -2$ mm and $d = +2$ mm, respectively. The lowest values of temperature overshoot and response delay concern the control implemented based upon the temperature assessed at d equal to 0 mm, i.e., 2.1 °C and 4.8 s.

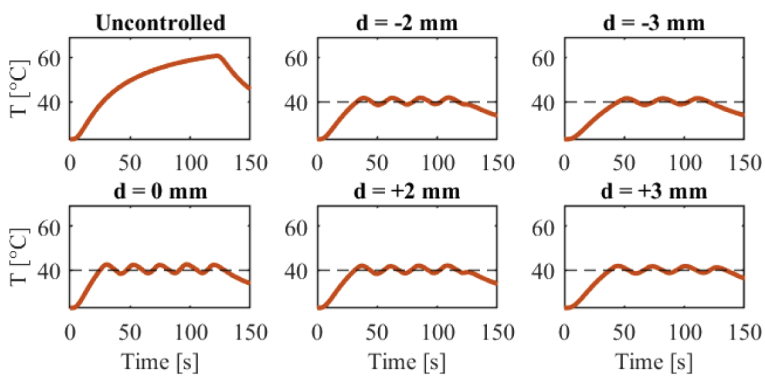

Fig. 6. Simulated temperature evolution obtained for the uncontrolled and the different temperature-controlled interstitial ablations in liver tissue. The dashed line indicates the set temperature T_S.

Figure 7 shows temperature distribution and the tissue volumes at 40 °C and 60 °C, for instance for LA controlled at $d = -3$ mm, and the associated maximum distances from the laser applicator axis at which temperatures corresponding to the setpoint and 60 °C extend, in case of overshoot. It can be noticed that, although temperatures of 40 °C can be found at larger distances ($r_{ext} = 0.91$ mm in case of overshoot, while $r_{ext} = 0.73$ mm when the laser is switched off), in case of overshoot (Fig. 7(a)) the inner tissue temperature results decreased compared to the heat

Biomedical Optics EXPRESS

distribution immediately before the laser is turned off (Fig. 7(b)). Indeed, temperatures ≥ 60 °C result more confined to the region closer to the laser tip.

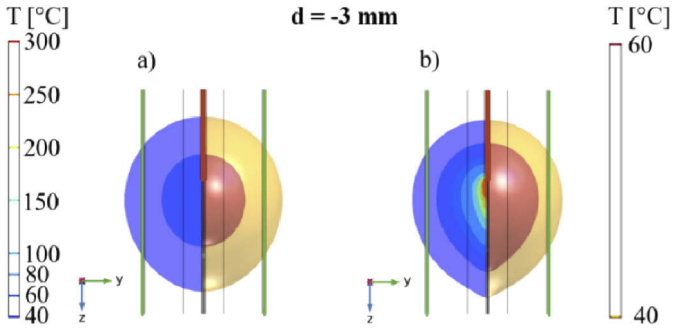

Fig. 7. Simulated temperature distribution and volumes of hepatic tissues at 40 °C and 60 °C concerning feedback-controlled LA at d = -3 mm, in case of (a) overshoot and (b) at the instant of time immediately before the laser source was turned off.

The thermal evolution during LA determines reversible and irreversible tissue changes, thus also irreversible tissue damage can occur. Figure 8 depicts the fraction of necrotic tissue attained in the different presented cases. The maximum fraction of necrotic tissue refers to the uncontrolled LA, i.e., 53 mm^3. Then, considering the same distances from the laser tip, fractions of necrotic tissue result larger in case of control performed based upon sensing locations placed behind the beam, compared to the ones positioned along the laser beam propagation direction. Hence, for d equal to -3 mm and -2 mm, the fractions of necrotic tissue are 34.4 mm^3 and 24.2 mm^3, respectively, while for d equal to +3 and +2 mm, necrotic tissues equal to 27.9 mm^3 and 23.0 mm^3, respectively. The minimum value is shown by the control actuated at d equal to 0 mm (21.1 mm^3). Table 3 reports the complete outlook of the results attained from the thermal analysis performed by means of the FEM-based simulation of laser-tissue interaction and the subsequent heat transfer in biological material.

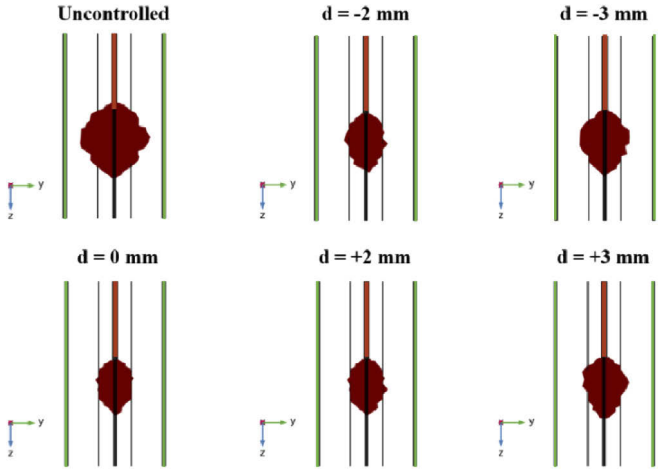

Fig. 8. Simulated fractions of necrotic tissue attained at the end of laser irradiation (laser exposure time of 120 s) for the different case-studies, i.e., uncontrolled treatment and temperature-controlled irradiation at different d values (see Visualization 1).

Biomedical Optics EXPRESS

Table 3. Overview of the results attained for the feedback-controlled laser interstitial irradiation simulation: the volumes of hepatic tissue characterized by temperatures ≥ 40 °C and ≥ 60 °C, immediately before the laser source was turned off for the first time, the temperature overshoots, the response delays, and the fractions of necrotic tissues are reported for the uncontrolled irradiation and the diverse control cases, based on the temperature assessed at the different *d* values.

	Uncontrolled	d = -3 mm	d = -2 mm	d = 0 mm	d = +2 mm	d = +3 mm
Volume [mm^3] at T ≥ 40 °C	509.2	276.3	192.8	155.9	175.7	225.6
Volume [mm^3] at T ≥ 60 °C	132.6	82.1	59.7	49.3	54.9	69.1
Overshoot [°C]	-	1.3	1.8	2.1	2.0	1.4
Response delay [s]	-	6.2	5.1	4.8	5.0	5.8
Fraction of necrotic tissue [mm^3]	53.0	34.4	24.2	21.1	23.0	27.9

4.2. Experimental results

After assessment of the thermal outcome at the set temperature T_S and diverse controlling distances with the implemented simulation, we performed *ex vivo* liver LA experiments with the defined input parameters to demonstrate the feasibility of the proposed LA control algorithm. In accordance with the simulations, T_S was set to 40 °C, and the d values were chosen equal to -3 mm, -2 mm, 0 mm, +2 mm, and +3 mm. Figure 9(a) reports the maximum temperatures measured by each FBG array during uncontrolled ablation. The difference in measured temperature profiles can be explained by sensor positioning uncertainties and inhomogeneities of the tissue. The temperature profiles for controlled cases are depicted in Fig. 9(b): temperatures on controlled z_d planes in the first column, and maximum measured temperatures (aligned to be on the z_0 plane) in the second column; while for the case of $d = 0$ mm, only one graph is presented because the controlled plane z_d lies in the z_0 plane. As it can be seen, the maximum temperature at z_d follows the set temperature value with some differences related to the ON-OFF control technique. Overshoot and delay response values are: 1.4 °C, 1 °C, 0.6 °C, 0.6 °C, and 1.4 °C; and 6.6 s, 4.2 s, 3.5 s, 2.2 s and 5 s for d equal to -3 mm, -2 mm, 0 mm, +2 mm, and +3 mm, correspondingly. The difference between measured temperature responses for the same distances in the backward and forward direction of the laser irradiation obtained during experiments validates the simulation results discussed in Section 4.1. This behavior can be explained by the fact that temperature rise behind the beam propagation direction is caused only by heat conduction and not by direct laser absorption. This phenomenon also can be appreciated in Fig. 10 (temperature profile evolution and associated contour maps showing the setpoint temperature value) for temperature profiles for the z_d planes reported in Fig. 9(b) (left column). Indeed, the plane z_0 and the planes with positive d have smoother temperature control and more spatially confined ablation regions.

The comparison between the simulated and the experimental results is presented in Fig. 11: the depicted maximum temperature profiles measured at the controlled z_d plane prove the feasibility of the simulation of ON-OFF control. Most of the simulations accurately predict the heating phase of ablation and its cooling trend. The difference in the controlling phase is mainly due to a phase shift of controlling actions. Overshoot and delay response values follow the trends discussed in the experimental section: 1.4 °C, 2.0 °C, 1.3 °C, 1.8 °C, and 2.1 °C, and 6.2 s, 5.1 s, 4.8 s, 5.0 s, and 5.8 s, for d equal to -3 mm, -2 mm, 0 mm, +2 mm, and +3 mm, correspondingly. The discrepancy for $d = +2$ mm can be explained by the possible inaccurate positioning of the sensor, which is also related to rapid temperature increase at z_0 at the beginning of ablation, as shown in Fig. 9(b) (blue line in the subplot $d = +2$ mm, referring to $T@z_0$). The high overshoot difference between simulation and experiments for z_0 can be explained by a stronger effect of laser absorption than heat conduction aspects.

Biomedical Optics EXPRESS

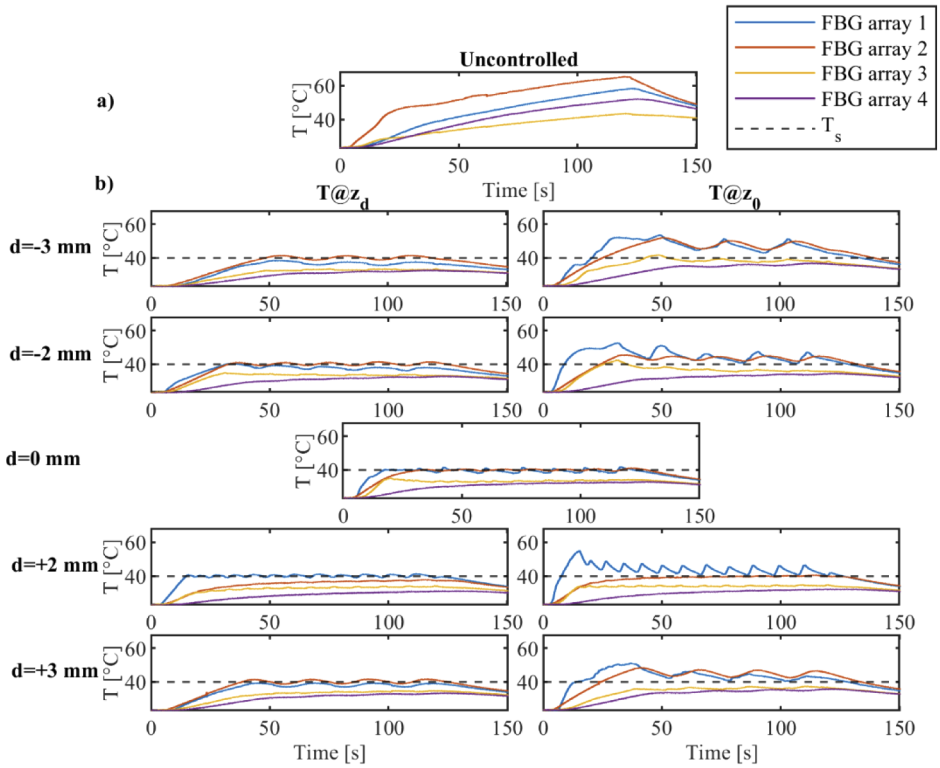

Fig. 9. Temperature profiles measured by four fiber Bragg grating (FBG) arrays during (a) uncontrolled ablation and (b) controlled ablation: the left column reports the temperature measured at z_d plane (controlled one), the right column depicts the temperature profiles at the z_0 plane (peak temperatures measured by FBG arrays) during the same experiment.

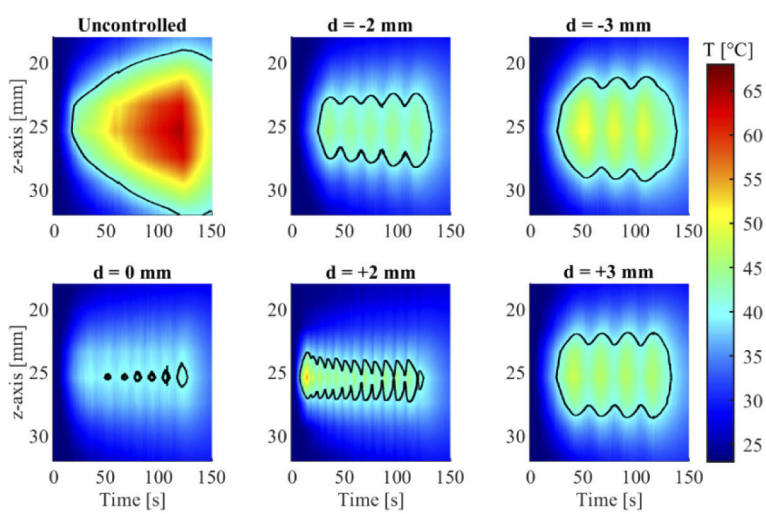

Fig. 10. Two-dimensional temperature map (time *vs.* distance along the controlled sensor positioned along the z-axis) attained through the FBG arrays measurements for the uncontrolled ablation treatment and the temperature feedback-controlled ablations: $T_s = 40$ °C, d = -3, -2, 0, +2, and +3 mm. The black contour lines define the region of hepatic tissue at temperature ≥ 40 °C.

Biomedical Optics EXPRESS

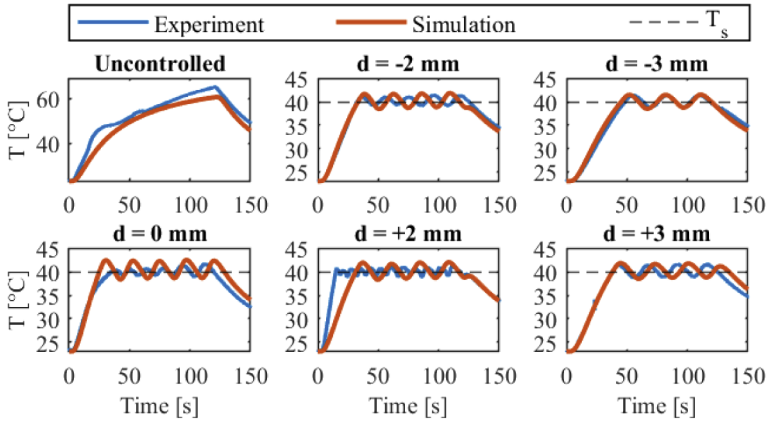

Fig. 11. Trends of uncontrolled LA and controlled temperature profiles obtained during LA experiments where the temperature was modulated based upon 40 gratings-highly dense FBG array measurements and comparison with temperature evolution attained with the FEM-based solver, adopted for solving the numerical model of the temperature-controlled interstitial LA procedure. The similarity of graphs validates the efficacy of the developed numerical model.

5. Discussion and conclusions

In this work, we theoretically and experimentally prove the feasibility of the use of highly dense FBG arrays for temperature-based control of interstitial LA. The interstitial approach leads to different possible fiber sensor arrangements in the ablated tissue and a variety of control methods for LA. We propose to use FBG arrays equidistant from the laser applicator to maintain stable temperatures at the margins of the treated region. A FEM-based simulation implemented in COMSOL Multiphysics is used to test pre-set parameters before the actual procedure and define the planned treatment in terms of peak temperature profiles, volumetric heat distribution, and fraction of the necrotic tissue. It is important to highlight that the volumetric and thermal damage evaluation is performed prior to treatment, while in real-time only temperature control at the specific plane is performed. The user interface of the developed LabVIEW program allows adjusting three input parameters (laser power, set temperature, and control distance) before the procedure, then LA control with real-time visualization of the measured temperature is performed. Simulation data were used to evaluate the overall ablation treatment and deal with a lack of volumetric temperature information stemmed from the inability to attain highly accurate 3D thermal maps with the utilized FBG arrays arrangement. According to numerical results, pre-set input parameters were chosen to contain the laser-induced thermal distribution (Figs. 4 and 6) in specific planes below the threshold values related to thermal damage process [45,46]. For the procedure with the tested input parameters, the fraction of necrotic tissue (Fig. 8) in the margins of the interested region was also calculated.

One of the main advantages of the proposed control approach is the use of highly dense FBG arrays. They provide several advantages over conventional measurement techniques for LA (i.e., thermistors, photo-optic probes, thermocouples, contactless thermometric systems) [23,47–49]: minimal invasiveness due to miniature dimensions of the fibers [26], low laser light absorption due to silica glass and polyimide material [34–36], reduced cost compared to other sensing techniques such as MRI-thermometry or fluoroptic sensors (e.g., approximately 50 $ considering a 1 mm sensitive length [50]), good metrological characteristics (i.e., response time in the order of 0.1 s and accuracy of <1 °C), and multipoint measurements derived from wavelength-division capabilities of FBG arrays [51]. These characteristics make FBG arrays

Biomedical Optics EXPRESS

well-suited for controlled interstitial ablation [14]. Indeed, previous studies employed mostly single-point metallic sensors for measuring and keeping the temperature at the desired threshold. Lin *et al*. used thermocouples to maintain the set temperature during *in vitro* experiments of photothermal therapy [49]. Moreover, an interstitial laser thermotherapy system constituted by an Nd:YAG laser and temperature feedback circuits embedding an automatic thermometry system based on single thermistor and thermocouple probes has been evaluated for *in vivo* LA in rats and on liver phantom [23]. Additionally, a temperature-controlled system based on thermocouple monitoring and a single low-power Nd:YAG laser for interstitial local hyperthermia has been implemented for the treatment of carcinoma [21]. The proposed sensors can suffer from self-heating once exposed to the NIR radiation due to the light absorption of metallic components [52,53]. Thus, leading to measurement errors that cannot be corrected during real-time temperature monitoring.

Regarding the capability of multipoint measurements of FBG arrays, Fig. 9 illustrates one of its main advantages for LA control, i.e., the ability to measure the temperature distribution and the position of its maximum that can change during the ablation procedure: the shift of the temperature maximum from one array to another during the LA procedure was properly detected for z_d=z_0 case. Moreover, the highly dense FBG arrays used in the experiments provide high spatial resolution that allows for accurate thermal map reconstruction (Fig. 10) during LA control. We observed that the sensor's position does not substantially affect the overshoot (1.4-1.6 °C) and the response delay (~2-7 s), but it influences the resulting temperature distribution. Experimental data also clearly show the efficacy of the control approach (Fig. 9), and the similarity with numerical results (Fig. 11).

The use of computational models for the simulation of the temperature-controlled ablation procedure has been already introduced by some authors. Ivarsson *et al*. report a temperature-controlled stepwise power regulation system for LA, based on thermistors with a spatial resolution of 10 mm. A numerical model based on the bioheat equation was also implemented to calculate the heat distribution, however, the thermal damage prediction was not included in the model [48]. Moreover, an auto-controlled laser on-off strategy was presented, combined with a theoretical model that numerically solved the heat diffusion equation, for retrieving the final volume heating, during photothermal therapy. In 2016, a feedback system based on a proportional-integrative-derivative (PID) control of thermocouple-assisted photothermal ablation performed with a 980 nm laser emitter was proposed [22]. In this work, the simulation model was implemented exploiting the Pennes' equation, solved by using a finite-element method. However, two different tuning approaches (manual and automatic, respectively) were utilized for computational modeling and the actual experimental treatment. Further studies proposed both the simulated and experimental assessment of temperature-controlled LA performed on *ex vivo* porcine liver by means of a thermographic measurement system. The heat distribution and the subsequent thermal injury were attained from the numerical simulation, however, the optical properties of untreated and coagulated tissue were not taken into consideration [29]. Moreover, a recently implemented work from the same research group referred to the maintenance of a set tissue temperature to induce the predetermined thermal coagulation on porcine liver tissue LA (1064 nm laser), using a thermocouple for real-time thermal monitoring [30].

Our analysis takes into account the change of tissue properties during LA according to the temperature and degree of tissue injury, and properly describes the thermal effects on the tissue, as witnessed by the comparable thermal outcomes attained in simulation and experimental frameworks (Fig. 11). This agreement validates the developed model and its use for preoperative optimization of LA parameters. In the future, this model could also be employed to perform an intraoperative control in combination with real-time measurement of the tissue changes. For instance, a potential technique that can monitor the transition state between native and coagulated tissue could also be applied [54]. The retrieved data might be used in the model

Biomedical Optics EXPRESS

for the estimation of the thermal outcome and the subsequent adjustment of the control settings during the procedure.

The ON-OFF control strategy used in our work allows, indeed, to effectively control the tissue temperature according to the set temperature, as also reported in other studies employing different thermal ablation techniques [55,56].

On the other hand, numerical and experimental results (Figs. 5, 6, 7, 9, and 11 and Table 3) demonstrate that the ON-OFF approach has some disadvantages, such as overshoot and delay response, that could affect the overall treatment [28]. Therefore, further evaluations on the effect of the wavelength and tissue optical properties could be of interest for assessing if overshoots and delay response can be limited, and new control techniques need to be introduced to improve treatment efficacy. For instance, a few studies [22,57] have been already investigating PID control for LA, but none of them considered quasi-distributed fiber sensors for PID-based control, which can be the future improvement of the proposed work for the optimal control of thermal effect during biological tissue LA. Lastly, being our analysis focused on the assessment of the validity of the theoretical model for pre-planning the control, a simplified and controllable approach neglecting the convective heat loss caused by blood perfusion was chosen. Indeed, the heat-sink effect has a significant impact on the temperature distribution in the target [58], hence future studies should also consider this phenomenon in both the pre-planning control strategy model and experiments, to approach the final clinical application. In order to implement our strategy in the *in vivo* conditions, other factors shall be considered in the future: a longer treatment time should be set to account for the thermal losses due to the concurrent blood perfusion; diffusing laser applicators could be employed to enlarge the treatment volume; the cross-sensitivity of FBGs to strain due to the physiological movements should be considered and possibly mitigated by the use of needles [59]; the position of sensors used for control should be tailored according to the tumor size, to attain the desired thermal damage.

Funding. European Research Council under the European Union's Horizon 2020 research and innovation programme (GA 759159).

Acknowledgment. This project has received funding from the European Research Council (ERC) under the European Union's Horizon 2020 research and innovation programme (Grant agreement No. 759159). The authors would like to acknowledge Alexey Wolf and Alexander Dostovalov at the Institute of Automation and Electrometry of the SB RAS, Novosibirsk (Russia) for producing FBG arrays for the measurements.

Disclosures. The authors declare no conflicts of interest.

Supplemental document. See Supplement 1 for supporting content.

References

1. H. P. Kok, E. N. K. Cressman, W. Ceelen, C. L. Brace, R. Ivkov, H. Grüll, G. ter Haar, P. Wust, and J. Crezee, "Heating technology for malignant tumors: a review," Int. J. Hyperthermia **37**(1), 711–741 (2020).
2. J. E. Kennedy, "High-intensity focused ultrasound in the treatment of solid tumours," Nat. Rev. Cancer **5**(4), 321–327 (2005).
3. R. Tateishi, S. Shiina, T. Teratani, S. Obi, S. Sato, Y. Koike, T. Fujishima, H. Yoshida, T. Kawabe, and M. Omata, "Percutaneous radiofrequency ablation for hepatocellular carcinoma," Cancer **103**(6), 1201–1209 (2005).
4. M. G. Lubner, C. L. Brace, J. L. Hinshaw, and F. T. Lee, "Microwave tumor ablation: mechanism of action, clinical results, and devices," J. Vasc. Interv. Radiol. **21**(8), S192–S203 (2010).
5. S. Natarajan, S. Raman, A. M. Priester, J. Garritano, D. J. A. Margolis, P. Lieu, M. L. Macairan, J. Huang, W. Grundfest, and L. S. Marks, "Focal Laser Ablation of Prostate Cancer: Phase I Clinical Trial," J. Urol. **196**(1), 68–75 (2016).
6. E. Schena, P. Saccomandi, and Y. Fong, "Laser ablation for cancer: past, present and future," J. Funct. Biomater. **8**(2), 19 (2017).
7. F. M. Di Matteo, P. Saccomandi, M. Martino, M. Pandolfi, M. Pizzicannella, V. Balassone, E. Schena, C. M. Pacella, S. Silvestri, and G. Costamagna, "Feasibility of EUS-guided Nd:YAG laser ablation of unresectable pancreatic adenocarcinoma," Gastrointest. Endosc. **88**(1), 168–174.e1 (2018).
8. R. J. Stafford, D. Fuentes, A. A. Elliott, J. S. Weinberg, and K. Ahrar, "Laser-induced thermal therapy for tumor ablation," Crit. Rev. Biomed. Eng. **38**(1), 79–100 (2010).
9. T. J. Vogl, R. Straub, K. Eichler, O. Söllner, and M. G. Mack, "Colorectal carcinoma metastases in liver: laser-induced interstitial thermotherapy—local tumor control rate and survival data," Radiology **230**(2), 450–458 (2004).

Biomedical Optics EXPRESS

10. H.-J. Schwarzmaier, F. Eickmeyer, W. von Tempelhoff, V. U. Fiedler, H. Niehoff, S. D. Ulrich, Q. Yang, and F. Ulrich, "MR-guided laser-induced interstitial thermotherapy of recurrent glioblastoma multiforme: preliminary results in 16 patients," Eur. J. Radiol. **59**(2), 208–215 (2006).
11. L. K. Swartz, K. G. Holste, M. M. Kim, A. Morikawa, and J. Heth, "Outcomes in patients treated with laser interstitial thermal therapy for primary brain cancer and brain metastases," Oncologist **24**(12), e1467–e1470 (2019).
12. R. Muschter, "Laser-induced interstitial thermotherapy of benign prostatic hyperplasia and prostate cancer," in *Medical Applications of Lasers II*, S. G. Bown, J. Escourrou, F. Frank, H. J. Geschwind, G. Godlewski, F. Laffitte, and H. H. Scherer, eds. (SPIE, 1994), 2327, pp. 287–292.
13. J. A. S. Brookes, W. R. Lees, and S. G. Bown, "Interstitial laser photocoagulation for the treatment of lung cancer," AJR, Am. J. Roentgenol. **168**(2), 357–358 (1997).
14. P. Saccomandi, E. Schena, M. A. Caponero, F. M. Di Matteo, M. Martino, M. Pandolfi, and S. Silvestri, "Theoretical analysis and experimental evaluation of laser-induced interstitial thermotherapy in ex vivo porcine pancreas," IEEE Trans. Biomed. Eng. **59**(10), 2958–2964 (2012).
15. Y. Kerbage, N. Betrouni, P. Collinet, H. Azaïs, S. Mordon, A.-S. Dewalle-Vignion, and B. Merlot, "Laser interstitial thermotherapy application for breast surgery: Current situation and new trends," The Breast **33**, 145–152 (2017).
16. A. J. Welch and M. J. C. Van Gemert, *Optical-Thermal Response of Laser-Irradiated Tissue* (Springer, 2011).
17. P. Saccomandi, E. Schena, and C. M. Pacella, "New horizons for laser ablation: nanomedicine, thermometry, and hyperthermal treatment planning tools," in *Image-Guided Laser Ablation* (Springer International Publishing, 2020), pp. 145–151.
18. K. F. Chu and D. E. Dupuy, "Thermal ablation of tumours: biological mechanisms and advances in therapy," Nat. Rev. Cancer **14**(3), 199–208 (2014).
19. S. A. Sapareto and W. C. Dewey, "Thermal dose determination in cancer therapy," Int. J. Radiat. Oncol., Biol., Phys. **10**(6), 787–800 (1984).
20. J. Pearce, "Mathematical models of laser-induced tissue thermal damage," Int. J. Hyperthermia **27**(8), 741–750 (2011).
21. N. Daikuzono, S. Suzuki, H. Tajiri, H. Tsunekawa, M. Ohyama, and S. N. Joffe, "Laserthermia: a new computer-controlled contact Nd:YAG system for interstitial local hyperthermia," Lasers Surg. Med. **8**(3), 254–258 (1988).
22. T. H. Nguyen, S. Park, K. K. Hlaing, and H. W. Kang, "Temperature feedback-controlled photothermal treatment with diffusing applicator: theoretical and experimental evaluations," Biomed. Opt. Express **7**(5), 1932 (2016).
23. P. H. Mollert, L. Lindbergt, P. H. Henriksson, and K. Tranberg, "Temperature control and light penetration in a feedback interstitial laser thermotherapy system," Int. J. Hyperthermia **12**(1), 49–63 (1996).
24. R. J. McNichols, A. Gowda, M. Kangasniemi, J. A. Bankson, R. E. Price, and J. D. Hazle, "MR thermometry-based feedback control of laser interstitial thermal therapy at 980 nm," Lasers Surg. Med. **34**(1), 48–55 (2004).
25. E. Schena, D. Tosi, P. Saccomandi, E. Lewis, and T. Kim, "Fiber optic sensors for temperature monitoring during thermal treatments: an overview," Sensors **16**(7), 1144 (2016).
26. F. Morra, M. De Landro, S. Korganbayev, A. Wolf, A. Dostovalov, A. Cigada, and P. Saccomandi, "Spatially resolved thermometry during laser ablation in tissues: distributed and quasi-distributed fiber optic-based sensing," Opt. Fiber Technol. **58**, 102295 (2020).
27. L. Bianchi, R. Mooney, Y. R. Cornejo, C. Hyde, E. Schena, J. M. Berlin, K. S. Aboody, and P. Saccomandi, "Fiber Bragg grating sensors for thermometry during gold nanorods-mediated photothermal therapy in tumor model," in *2020 IEEE Sensors* (IEEE, 2020), pp. 1–4.
28. S. Korganbayev, A. Orrico, L. Bianchi, M. De Landro, A. Wolf, A. Dostovalov, and P. Saccomandi, "Closed-loop temperature control based on fiber Bragg grating sensors for laser ablation of hepatic tissue," Sensors **20**(22), 6496 (2020).
29. V. N. Tran, V. G. Truong, S. Jeong, and H. W. Kang, "Computational analysis of linear energy modulation for laser thermal coagulation," Biomed. Opt. Express **9**(6), 2575 (2018).
30. V. N. Tran, V. G. Truong, Y. W. Lee, and H. W. Kang, "Effect of optical energy modulation on the thermal response of biological tissue: computational and experimental validations," Biomed. Opt. Express **11**(12), 6905 (2020).
31. S. R. Guntur, K. Il Lee, D.-G. Paeng, A. J. Coleman, and M. J. Choi, "Temperature-dependent thermal properties of ex vivo liver undergoing thermal ablation," Ultrasound Med. Biol. **39**(10), 1771–1784 (2013).
32. J. P. Ritz, A. Roggan, C. Isbert, G. Mller, H. J. Buhr, and C. T. Germer, "Optical properties of native and coagulated porcine liver tissue between 400 and 2400 nm," Lasers Surg. Med. **29**(3), 205–212 (2001).
33. B. Cox, "Introduction to laser-tissue interactions," PHAS **4886**, 1–61 (2007).
34. K. Weir, "Optical fiber sensor technology," J. Mod. Opt. **42**(4), 938 (1995).
35. L. Huang, R. S. Dyer, R. J. Lago, A. A. Stolov, and J. Li, "Mechanical properties of polyimide coated optical fibers at elevated temperatures," Proc. SPIE **9702**, 97020Y (2016).
36. A. V. Dostovalov, A. A. Wolf, A. V. Parygin, V. E. Zyubin, and S. A. Babin, "Femtosecond point-by-point inscription of Bragg gratings by drawing a coated fiber through ferrule," Opt. Express **24**(15), 16232–16237 (2016).
37. S. Korganbayev, R. Pini, A. Orrico, A. Wolf, A. Dostovalov, and P. Saccomandi, "Towards temperature-controlled laser ablation based on fiber Bragg grating array temperature measurements," in *2020 IEEE International Workshop on Metrology for Industry 4.0 and IoT, MetroInd 4.0 and IoT 2020 - Proceedings* (2020).

Biomedical Optics EXPRESS

38. S. Nomura, M. Arake, Y. Morimoto, H. Tsujimoto, H. Miyazaki, D. Saitoh, N. Shinomiya, K. Hase, J. Yamamoto, and H. Ueno, "Thermal sensor circuit using thermography for temperature-controlled laser hyperthermia," J. Sensors **2017**, 1–7 (2017).
39. M. H. Niemz, *Laser-Tissue Interactions*, Biological and Medical Physics, Biomedical Engineering (Springer, 2007).
40. A. Ishimaru, "Diffusion of light in turbid material," Appl. Opt. **28**(12), 2210 (1989).
41. Y. Mohammed and J. F. Verhey, "A finite element method model to simulate laser interstitial thermo therapy in anatomical inhomogeneous regions," Biomed. Eng. Online **4**(1), 2 (2005).
42. C. Multiphysics, "Heat Transfer Module," Manual 1–222 (2015).
43. D. K. Sardar, A. Sayka, and R. M. Yow, "Characterization of optical properties of polyimide precursors," Semicond Manuf (Web Exclus.) **8**, 1–5 (2007).
44. S. N. Goldberg, G. S. Gazelle, and P. R. Mueller, "Thermal ablation therapy for focal malignancy," Am. J. Roentgenol. **174**(2), 323–331 (2000).
45. S. Thomsen, "Pathologic analysis of photothermal and photomechanical effects of laser-tissue interactions," Photochem. Photobiol. **53**(6), 825–835 (1991).
46. V. K. Nagarajan, J. M. Ward, and B. Yu, "Association of liver tissue optical properties and thermal damage," Lasers Surg. Med. **52**(8), 779–787 (2020).
47. W. A. Wohlgemuth, È. Wamser, T. Reiss, and T. Wagner, "In vivo laser-induced interstitial thermotherapy of pig liver with a temperature-controlled diode laser and MRI correlation," Lasers Surg. Med. **29**(4), 374–378 (2001).
48. K. Ivarsson, J. Olsrud, and C. Sturesson, "Feedback interstitial diode laser (805 nm) thermotherapy system: ex vivo evaluation and mathematical modeling with one and four-fibers," Lasers Surg. Med. **22**(2), 86–96 (1998).
49. J.-T. Lin, Y.-S. Chiang, G.-H. Lin, H. Lee, and H.-W. Liu, "In vitro photothermal destruction of cancer cells using gold nanorods and pulsed-train near-infrared laser," J. Nanomater. **2012**, 1–6 (2012).
50. D. Polito, M. Arturo Caponero, A. Polimadei, P. Saccomandi, C. Massaroni, S. Silvestri, and E. Schena, "A needlelike probe for temperature monitoring during laser ablation based on fiber bragg grating: manufacturing and characterization," J. Med. Devices **9**(4), 041006 (2015).
51. T. Erdogan, "Fiber grating spectra," J. Lightwave Technol. **15**(8), 1277–1294 (1997).
52. P. Saccomandi, E. Schena, and S. Silvestri, "Techniques for temperature monitoring during laser-induced thermotherapy: An overview," Int. J. Hyperthermia **29**(7), 609–619 (2013).
53. F. Manns, P. J. Milne, X. Gonzalez-Cirre, D. B. Denham, J. Parel, and D. S. Robinson, "In situ temperature measurements with thermocouple probes during laser interstitial thermotherapy (LITT): quantification and correction of a measurement artifact," Lasers Surg. Med. **23**(2), 94–103 (1998).
54. P. Lanka, F. Kalloor Joseph, H. Kruit, S. Konugolu Venkata Sekar, A. Farina, R. Cubeddu, S. Manohar, and A. Pifferi, "Monitoring radiofrequency ablation of biological tissue using broadband time-resolved diffuse optical spectroscopy," in *Diffuse Optical Spectroscopy and Imaging VII*, H. Dehghani and H. Wabnitz, eds. (SPIE, 2019), p. 94.
55. M. Li, X. Yu, P. Liang, F. Liu, B. Dong, and P. Zhou, "Percutaneous microwave ablation for liver cancer adjacent to the diaphragm," Int. J. Hyperthermia **28**(3), 218–226 (2012).
56. M. Trujillo, J. Bon, M. José Rivera, F. Burdío, and E. Berjano, "Computer modelling of an impedance-controlled pulsing protocol for RF tumour ablation with a cooled electrode," Int. J. Hyperthermia **32**(8), 931–939 (2016).
57. X. Feng, F. Gao, C. Xu, L. Gaoming, and Y. Zheng, "Self temperature regulation of photothermal therapy by laser-shared photoacoustic feedback," Opt. Lett. **40**(19), 4492–4495 (2015).
58. E. De Vita, M. De Landro, C. Massaroni, A. Iadicicco, P. Saccomandi, E. Schena, and S. Campopiano, "Fiber optic sensors-based thermal analysis of perfusion-mediated tissue cooling in liver undergoing laser ablation," IEEE Trans. Biomed. Eng. **68**(3), 1066–1073 (2021).
59. C. Cavaiola, P. Saccomandi, C. Massaroni, D. Tosi, F. Giurazza, G. Frauenfelder, B. Beomonte Zobel, F. M. Di Matteo, M. A. Caponero, A. Polimadei, and E. Schena, "Error of a temperature probe for cancer ablation monitoring caused by respiratory movements: *ex vivo* and *in vivo* analysis," IEEE Sens. J. **16**(15), 5934–5941 (2016).